J. Plasma Physics (2001), *vol.* 66, *part* 4, *pp.* 275–294. © 2001 Cambridge University Press
DOI: 10.1017/S0022377801001416 Printed in the United Kingdom

Magnetic relaxation in spheromaks using spectral expansions in cylindrical geometry

DANIEL D. HUA, T. KENNETH FOWLER
and EDWARD C. MORSE

Department of Nuclear Engineering, University of California, Berkeley, CA, USA

(Received 24 October 2000 and in revised form 16 July 2001)

Abstract. A code has been developed to study self-organization in spheromaks using the Galerkin method in which the magnetic and velocity fields appearing in the incompressible dissipative MHD equations are expanded in a spectrum of Chandrasekhar–Kendall eigenstates of the curl. The ultimate goal is to apply the Galerkin method in actual spheromak geometry to calculate turbulence levels and associated transport. The present work employs the straight-cylinder approximation, known to give a good representation of internal ideal MHD modes in spheromaks and applied here to resistive tearing modes. Our main result to date is a demonstration that the Galerkin method can exhibit tearing island formation with only a few states in the spectrum. Example quasilinear calculations are presented for a decaying spheromak and for a spheromak created by gun injection.

1. Introduction

The main feature of spheromak experiments appears to be self-organization by continuous relaxation toward a preferred magnetic state (Jarboe 1994). Taylor's minimum-energy theory of magnetic self-organization predicts that helicity injection by magnetized Marshall guns commonly used to create spheromaks in the laboratory should both produce and sustain the 'flux core' spheromak configuration shown in Fig. 1 (Taylor 1986). The gun might do this by repeatedly driving current in the open-line flux core above an instability threshold, thereby generating magnetic fluctuations (e.g. resistive tearing modes) that propagate helicity out of the flux core into the surrounding spheromak (Jensen and Chu 1984).

If the system does relax and if the relaxed state is known (e.g. the Taylor state), it is possible to derive the time-averaged fluctuation levels required to maintain the relaxed state and from this to estimate heat diffusion coefficients due to the fluctuations. We have had some success using this diffusion model to explain temperature measurements in the CTX spheromak experiment at Los Alamos (Fowler and Hua 1995), and a transport code using this model predicts attractive operating scenarios for Ohmically ignited steady-state and pulsed spheromak fusion reactors (Fowler et al. 1999).

The present work grew out of our desire to devise a simple method to calculate fluctuations directly rather than by our indirect method assuming relaxation to the Taylor state. For this, we turned to the Galerkin method, in which the magnetic and velocity fields appearing in dissipative MHD theory are expanded in

https://doi.org/10.1017/S0022377801001416 Published online by Cambridge University Press

a truncated spectrum of Chandrasekhar–Kendall eigenstates of the curl operator (Chandrasekhar and Kendall 1957). Application of the Galerkin method in fusion research was pioneered by Montgomery and co-workers (Shan et al. 1991; Shan and Montgomery 1993a, b). The above references discuss the advantages and disadvantages of the Galerkin approach for MHD problems. It is especially important that, for zero dissipation, the Galerkin method conserves both energy and helicity exactly, regardless of the truncation of the spectrum into any finite number of retained eigenstates.

Motivated by success in calculating ideal MHD stability by eigenstate expansions in realistic spherical geometry (Morse 1998), we first attempted to study spheromak relaxation in spherical geometry (Hua et al. 1998), but we became concerned about whether or not the Galerkin method was able to resolve tearing modes correctly. The work presented here was undertaken to help us understand the tearing mode using a simpler straight-cylinder approximation already shown to give good agreement with spherical geometry for ideal MHD stability (Jardin 1982).

Our most important result to date is a demonstration that the Galerkin method can calculate tearing modes with a manageable number of eigenstates. The theoretical basis for this is discussed in Sec. 6, with benchmark calculations in Sec. 7. The eigenstate representation in cylindrical geometry is discussed in Secs 2–5. Examples of quasilinear calculations are presented for a decaying spheromak in Sec. 8 and for a spheromak created by gun injection in Sec. 9.

2. Review of spectral representation of turbulence

We describe the spheromak by incompressible, dissipative MHD equations in the limit of small flow velocity $\mathbf{v}$. Dropping terms quadratic in $\mathbf{v}$, the field and momentum equations are given by

$$\frac{\partial \mathbf{B}}{\partial t} = \boldsymbol{\nabla} \times (\mathbf{v} \times \mathbf{B} - \eta \mathbf{J}), \tag{2.1}$$

$$\frac{\partial \boldsymbol{\nabla} \times \mathbf{v}}{\partial t} = (\rho \mu_0)^{-1} \boldsymbol{\nabla} \times (\mathbf{J} \times \mathbf{B} - \nu \boldsymbol{\nabla} \times \boldsymbol{\nabla} \times \mathbf{v}), \tag{2.2}$$

with constant density ρ, resistivity η and viscosity ν. Note that we have taken the curl of (2.2) to eliminate $\boldsymbol{\nabla} p$, and $\boldsymbol{\nabla} \times \boldsymbol{\nabla} \times \mathbf{v} \equiv -\nabla^2 \mathbf{v}$ since $\boldsymbol{\nabla} \cdot \mathbf{v} = 0$. As discussed in Sec. 1, we project these equations onto the Chandrasekhar–Kendall eigenstates of the curl:

$$\mathbf{B} = \sum_i a_i \mathbf{B}_i, \tag{2.3}$$

$$\mathbf{v} = \sum_i v_i \mathbf{B}_i, \tag{2.4}$$

where

$$\boldsymbol{\nabla} \times \mathbf{B}_i = \lambda_i \mathbf{B}_i. \tag{2.5}$$

Here i is a state label defined in Sec. 3.

Using the orthogonality of the $\mathbf{B}_i$, (2.1) and (2.2) can be transformed as

$$\frac{\partial a_i}{\partial t} = \sum_{j,j} \lambda_i v_j a_k M_{ijk} - \eta \lambda_i^2 a_i, \tag{2.6}$$

$$\frac{\partial v_i}{\partial t} = \sum_{i,j} \lambda_j a_j a_k M_{ijk} - \nu \lambda_i^2 v_i, \tag{2.7}$$

https://doi.org/10.1017/S0022377801001416 Published online by Cambridge University Press

where

$$M_{ijk} = \int dV\, \mathbf{B}_i \cdot \mathbf{B}_j \times \mathbf{B}_k, \tag{2.8}$$

with normalized $\mathbf{B}_i$ such that $\int \mathbf{B}_i \cdot \mathbf{B}_i\, dV = 1$. Units take the cylinder radius $a = 1$, the magnetic unit B is arbitrary corresponding to $a_i = 1$, and time is in Alfvén transit times for this value of B. Then $\eta = S^{-1}$, where S is the Lundquist number and $\nu = R_m/(S\,Re)$ for Reynolds number Re and magnetic Reynolds number R_m.

The summations in (2.6)–(2.8) run over the state labels for any truncated set of curl eigenstates chosen to represent the system. As noted earlier, for any such representation, (2.6)–(2.8) conserve energy E and helicity K when $\nu = 0$ and $\eta = 0$. E and K are given by

$$E = \tfrac{1}{2} \sum_i (a_i^2 + v_i^2), \tag{2.9}$$

$$K = \int dV\, \mathbf{A} \cdot \mathbf{B} = \sum_i \lambda_i^{-1} a_i^2. \tag{2.10}$$

To prove conservation of energy and helicity for the non-dissipative case, we differentiate (2.9) and (2.10) using (2.6) and (2.7) with $\eta = 0$ and $\nu = 0$ to obtain

$$\frac{dE}{dt} = \sum_{ijk} (a_i \lambda_i v_j a_k + v_i \lambda_j a_j a_k) M_{ijk} = 0, \tag{2.11}$$

$$\frac{dK}{dt} = \sum_{ijk} a_i v_j a_k M_{ijk} = \int d^3V\, \mathbf{B} \cdot \mathbf{v} \times \mathbf{B} = 0. \tag{2.12}$$

In (2.11), the cancelation is obtained by swapping state labels i and j in the second term and using $M_{jik} = -M_{ijk}$ by the cyclic property of the triple product in (2.8). Equation (2.12) follows by noting that λ_i^{-1} in (2.10) has been cancelled by the λ_i term in da_i/dt, giving a summation that can be reassembled into a vector product that is manifestly zero. We will use the conservation laws to test the accuracy of our integrations of (2.6) and (2.7) in Secs 8 and 9.

Note the simplicity of representing the reduced MHD theory in (2.1) and (2.2) by curl eigenstates whereby every curl operator is replaced by an eigenvalue and the extra curl operation that eliminates $\boldsymbol{\nabla} p$ in (2.2) factors out. The curl representation of the velocity field implies incompressible flow with $\boldsymbol{\nabla} \cdot \mathbf{v} = 0$, since $\mathbf{v}$ in (2.4) is purely rotational. This is not always valid in spheromaks, as we could discover by tracking the divergence of the momentum equation, but we will not do so here.

3. Eigenstates in the straight-cylinder approximation

For reasons discussed in Sec. 1, we will approximate the spheromak by a straight cylinder of radius a and length $2\pi a$ parallel to the magnetic axis (aspect ratio 1). Then B_z along the cylindrical axis represents the toroidal field of the spheromak. Figure 1 illustrates the geometric model. Following Jardin (1982), we expect this to give a reasonable representation of the closed spheromak core itself but not the open-line flux core, a point to which we will return in Sec. 9.

For the straight-cylinder geometry, the Chandrasekhar–Kendall eigenstates

https://doi.org/10.1017/S0022377801001416 Published online by Cambridge University Press

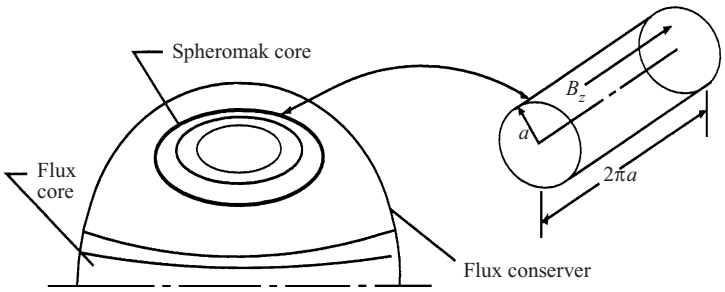


Figure 1. Application of straight-cylindrical geometry to a spheromak.

(taken as real) have the form

$$B_r = \mathscr{B}^{-1}\left[\frac{m\lambda^2}{k_r\rho}J_m(\rho) + \frac{k_z\lambda}{k_r}J'_m(\rho)\right] \times[A\cos(k_z z + m\theta) + B\sin(k_z z + m\theta)], \tag{3.1a}$$

$$B_\theta = \mathscr{B}^{-1}\left[\frac{mk_z\lambda}{k_r\rho}J_m(\rho) + \frac{\lambda^2}{k_r}J'_m(\rho)\right] \times[-A\sin(k_z z + m\theta) + B\cos(k_z z + m\theta)], \tag{3.1b}$$

$$B_z = \mathscr{B}^{-1}[\lambda J_m(\rho)][A\sin(k_z z + m\theta) - B\cos(k_z z + m\theta)], \tag{3.1c}$$

$$\mathscr{B}^2 = \lambda^2\pi L\left\{\frac{(\lambda + k_z)^2}{4k_r^2}[J^2_{m-1}(k_r) - J_{m-2}(k_r)J_m(k_r)] + \frac{(\lambda - k_z)^2}{4k_r^2}[J^2_{m+1}(k_r) - J_{m+2}(k_r)J_m(k_r)] + \tfrac{1}{2}[J^2_m(k_r) - J_{m-1}(k_r)J_{m+1}(k_r)]\right\}, \tag{3.1d}$$

where $\rho = k_r r$, a prime indicates differentiation with respect to ρ, $\mathscr{B}$ is the normalization constant, and λ is given by

$$\lambda^2 = k_r^2 + k_z^2. \tag{3.2}$$

Note that we have multiplied eigenfunctions by an extra factor λ, for reasons explained below.

Equation (3.1) defines two classes of real eigenstates (two parities), with positive parity being given by setting $A = 1$ and $B = 0$, and negative parity by setting $A = 0$ and $B = 1$. Otherwise eigenstates can be specified by three quantum numbers: λ (or k_r), m and $n = k_z L/2\pi$, with periodic boundary conditions in θ and z so that m and n are integers. (We defer the discussion of boundary conditions on k_r to the next section.) Thus each curl eigenstate has associated with it four identifying labels: the parity label plus three quantum numbers λ, m, n. These eigenstates are orthonormal, giving $\int dV\, \mathbf{B}_i \cdot \mathbf{B}_j = 1$ if the parity and all quantum numbers in state i are the same as those in state j, and zero otherwise. In particular, perturbation states of positive parity are orthogonal to states of negative parity due to mixing of sines and cosines. We will use these eigenstate properties in evaluating the matrix elements.

A word about notation: in the preceding paragraph, the state labels i and j, like the labels i, j, k on eigenstates and matrices in Sec. 2, are 'counting labels', each

https://doi.org/10.1017/S0022377801001416 Published online by Cambridge University Press

state label being identified with a set of four parity and quantum number labels required to specify that eigenstate.

4. Choice of spectrum and calculation of matrix elements

The matrix elements M_{ijk} in the dynamical equations (2.6) and (2.7) are uniquely determined for any set of eigenstates chosen to represent the system. The issue, of course, is how to choose a set of states that economically captures the physics of interest.

For guidance, we follow the traditional approach in fusion research of identifying the symmetric magnetic states with $m = n = 0$, or sums of these states, as 'equilibria,' and non-symmetric states as 'perturbations'. Any sum of symmetric magnetic eigenstates is an 'equilibrium' in the usual sense that it satisfies (2.6) and (2.7) in steady state with zero flow ($\mathbf{v} = 0$) and zero dissipation ($\eta = \nu = 0$), by properties of the matrix elements (item (b) below). However, there is nothing to prevent the nonlinear evolution of our 'equilibrium' to a non-symmetric state in which $\mathbf{v}$ is finite and magnetic 'perturbations' are large, and we shall find examples of this.

To approximate a spheromak confined in a flux conserver with perfectly conducting walls, we take the cylinder aspect ratio $L/2\pi a$ to be unity as already noted, and we require $B_r = 0$ at the wall. For the perturbations, this boundary condition determines k_r for these states (and λ, by (3.2)). For symmetric states, for which $B_r = 0$ by symmetry, we impose the additional requirement that $B_z = 0$ at the wall, which then determines k_r for these states. This requirement follows because the toroidal field in a symmetric spheromak is produced solely by poloidal current within the plasma. It is this fact that distinguishes a spheromak from a reversed-field pinch (RFP) with a negative toroidal field at the wall (due to coils or image currents) and a tokamak with a strong positive toroidal field outside. The aspect ratio of unity further distinguishes the straight-cylinder approximation to a spheromak from that for an RFP at zero field reversal.

In the straight-cylinder approximation of the spheromak, the Taylor state of minimum energy is a symmetric state with $\lambda = 2.405$ (first zero of $J_0(k_r r)$, units $a = 1$). While this state and all of the symmetric eigenstates with constant λ are force-free with zero pressure, a sum of such states having different eigenvalues can represent an equilibrium with finite pressure (Morse 1998). In the cylindrical model, $\mathbf{j} \times \mathbf{B}$ is always radial for symmetric states, thus allowing us to make the interpretation $\mathbf{j} \times \mathbf{B} = \boldsymbol{\nabla} p$ to obtain the pressure:

$$p = \int_r^1 dr\, (\mathbf{j} \times \mathbf{B})_r \tag{4.1}$$

Incidentally, one can show that the extra factor of λ in (3.1) mentioned earlier is a convenient way to guarantee $p \geqslant 0$; it was introduced for this reason. In the applications in Secs 8 and 9, we will be guided in our choice of symmetric states in the spectrum to give values of $\beta = 2\mu_0 p/B^2$ of experimental interest and to construct realistic profiles of $\lambda_\parallel = \mu_0 j_\parallel / B$ from a sum of symmetric eigenstates.

To select perturbations, we seek states that might destabilize our equilibria, with matrix elements M_{ijk} large enough to influence solutions of the dynamical equations (2.6) and (2.7). These matrix elements are uniquely determined for any set of eigenstates chosen to represent the system. The M_{ijk} are calculated by (2.8) using the symbolic algebra program *Maple V*.

https://doi.org/10.1017/S0022377801001416 Published online by Cambridge University Press

Table 1. Eigenvalues λ, radial wavenumbers k_r, normalization constants $\mathscr{B}^2$ and interaction coefficients M_{ijk} for some selected states (with state labels in the first column).

State	λ	m	n	Parity	$\mathscr{B}^2$
1	2.405	0	0	(−)	61.53
2	−2.405	0	0	(−)	61.53
3	5.520	0	0	(−)	139.28
4	4.668	1	−1	(+)	60.64
5	7.832	1	−1	(−)	99.68
6	10.981	1	−1	(+)	138.92
7	5.237	1	−2	(+)	79.53
8	3.137	1	1	(+)	44.27
9	58.117	1	−1	(−)	730.51

$M_{\mathbf{145}} = -M_{\mathbf{415}} = 2.881 \times 10^{-3}$, $M_{\mathbf{245}} = -M_{\mathbf{542}} = -1.489 \times 10^{-2}$
$M_{\mathbf{345}} = -6.836 \times 10^{-2}$, $M_{\mathbf{149}} = 5.954 \times 10^{-7}$

Some useful properties of the triple product M_{ijk} are as follows:

(a) The vector product in M_{ijk} is cyclic, giving $M_{ijk} = M_{kij} = -M_{jik}$.

(b) $M_{ijk} = 0$ when i, j, and k are all symmetric states, since for these states $\mathbf{B}_i \times \mathbf{B}_j$ has only a radial component, giving a zero dot product with a third symmetric state. Equations (2.6) and (2.7) always couple symmetric states to perturbation states. This property guarantees that symmetric equilibria satisfy the equations of motion with zero flow and dissipation, as noted above.

In this paper, we consider only $m = 1$ perturbation states (known to give the largest growth constants), leading to the following additional constraints to obtain non-zero matrix elements:

(c) Non-zero M_{ijk} must contain one and only one symmetric ($m = n = 0$) state. Then, for perturbation states, (2.6) and (2.7) are linearized, which is to say our nonlinear calculations are carried out in the quasilinear approximation.

(d) The two non-symmetric states must have the same m and n. For example, the three states could take the form (identifying states by their quantum numbers) $(\lambda_i, 0, 0), (\lambda_j, m, n)$ and (λ_k, m, n).

(e) If one non-symmetric state has positive parity, the other must have negative parity.

(f) $|M_{ijk}| \to 0$ monotonically as $|\lambda_i - \lambda_j - \lambda_k| \to \infty$, and M_{ijk} is maximized when the λ have neighboring values.

Full nonlinear mode coupling could, of course, be included by using M_{ijk} involving three perturbations with m and n values satisfying the equivalent of the $\sum \mathbf{k} = 0$ selection rule in the usual three-wave theory. But we will not do this here.

Table 1 lists examples of eigenstates in straight-cylinder geometry used in later calculations, together with their eigenvalues and normalization constants, and representative matrix elements coupling these states.

We defer to Secs 7 and 8 a discussion of the stability properties of this choice of states.

https://doi.org/10.1017/S0022377801001416 Published online by Cambridge University Press

5. Code development

A spectral code has been written that solves the nonlinear coupled ordinary differential equations in (2.6) and (2.7) for a chosen set of eigenstates and interaction coefficients M_{ijk} calculated as described above. The equations are numerically integrated using a Runge–Kutta scheme from the Numerical Algorithm Group (NAG) FORTRAN library, D02PCF.

The number of states in the spectrum depends on three factors. First is the number of symmetric states required to give equilibria of interest, typically three states in our examples below. Second is the number of magnetic 'resonances' included, a resonant flux surface occurring if the safety factor $q(r) = -m/n$ for quantum numbers m and n, as in other toroidal confinement devices. Finally, and most importantly for the Galerkin method, is the number of radial perturbation states required to resolve magnetic island structures around these resonances, typically 19 perturbation states for each pair of m and n values.

Nineteen radial perturbation states per resonance are chosen based on benchmark studies discussed in Sec. 7. We typically treat three resonances, giving $3 \times 19 = 57$ magnetic perturbation equations and 57 velocity equations, plus 6 equilibrium equations, for a total of 120 equations. Thirteen radial states yields essentially the same nonlinear results, but still requires 84 equations.

6. Identification of tearing modes

Preliminary to using this nonlinear code, we have compared the linearized spectral theory with known analytic results, with equilibria given by an expansion in symmetric eigenstates independent of θ and z. On linearizing (2.6) and (2.7) about this equilibrium, the matrix elements contain one contribution from an equilibrium state component, which can always be rotated to the leftmost position in (2.8), leaving a cross product of perturbations $\mathbf{B}_j \times \mathbf{B}_k$ as the projection of the equations onto the ith eigenstate. Both m and k_z are good quantum numbers for the linearized equations, giving linearized solutions depending on a single value of $\omega \equiv k_z z + m\theta$ with both $\cos\omega$ and $\sin\omega$ terms for each eigenvalue. The cross product mixes sines and cosines, giving for (2.6) a matrix $\mathbf{B}$ of the form

$$\mathbf{B} = \begin{pmatrix} 0 & X & 0 & \dots \\ X & 0 & X & \dots \\ 0 & X & 0 & \dots \\ \dots & & & \end{pmatrix}, \tag{6.1}$$

and a matrix $\mathbf{V}$ of the same form for (2.7). Here rows and columns are labeled by λ (or k_r), alternating between cosine and sine. It can be shown that, for odd dimension N, matrices of this form always have one zero eigenvalue, from which the matrix product $\delta\mathbf{W} = \mathbf{BV}$ has a pair of zero eigenvalues, with determinant of the form

$$\det \delta\mathbf{W} = p^2 \left(p^{2N-2} + \cdots \sum_{i=1}^{N} K_i \right) = 0. \tag{6.2}$$

with time dependence $\exp(pt)$.

The matrix $\delta\mathbf{W}$ is the Galerkin counterpart to the usual energy perturbation $\delta\mathbf{W}$ in ideal MHD stability theory. We expect resistive tearing modes to occur around a zero eigenvalue of $\delta\mathbf{W}$ when the perturbation spectrum allows breaking of field

https://doi.org/10.1017/S0022377801001416 Published online by Cambridge University Press

lines (Rosenbluth and Rutherford 1981). We have indeed shown by a succession of computer calculations for a small, odd N that adding a small constant resistivity η causes the $p^2 = 0$ roots of (6.2) to split into one with $p = 0$ and another that is proportional to η, this being the resistive mode. This resistive root always occurs, independent of the magnitude of matrix elements. The other roots, obtained by setting $\{\ldots\} = 0$, are the ideal MHD modes.

The root structure for a small number of states shows a strong 'odd–even effect', whereby even N produces significantly different behavior than odd N for small N. This behavior can be traced to the sign of the error induced by the representation of the bilinear terms in the equations shown above by the eigenfunctions retained in the space, and thus a sort of aliasing effect. For large N, the odd–even behavior becomes insignificant, and the solutions for small odd N are closer to the large-N case than for small even N. The convergence properties of Galerkin-type solutions to dynamical systems with elliptic spatial operators for MHD simulation are well studied (Patterson and Orszag 1971; Shebalin and Montgomery 1988).

The way in which resistivity perturbs the zero roots can be seen from the example of three perturbative states, for which the matrix $\delta\mathbf{W}$ takes the form

$$\delta\mathbf{W} = \begin{pmatrix} B_{12}V_{21} & 0 & B_{12}V_{23} \\ 0 & B_{21}V_{12} + B_{23}V_{32} & 0 \\ B_{32}V_{21} & 0 & B_{32}V_{23} \end{pmatrix}. \tag{6.3}$$

Substituting this into the combined equations (2.6) and (2.7) with constant resistivity gives for the upper and lower rows equations of the form

$$p(p + \eta\lambda_1^2)a_1 = B_{12}V_{21}a_1 + B_{12}V_{23}a_3, \tag{6.4}$$

$$p(p + \eta\lambda_3^2)a_3 = B_{32}V_{21}a_1 + B_{32}V_{23}a_3, \tag{6.5}$$

where the factors λ^2 arise from matrix elements of $\boldsymbol{\nabla} \times \eta\mathbf{J}$ (one factor of λ coming from the curl and another from $\mathbf{J} = \lambda\mathbf{B}$). Solving gives

$$p[p(p + \eta\lambda_1^2)(p + \eta\lambda_3^2) - (p + \eta\lambda_1^2)B_{32}V_{23} - (p + \eta\lambda_3^2)B_{12}V_{21}] = 0, \tag{6.6}$$

where terms independent of p have canceled. For finite η, (6.6) has one $p = 0$ root due to the factor out front and another (the resistive mode) found by dropping the higher-order terms, giving

$$p = \frac{-\eta(\lambda_1^2 B_{32}V_{23} + \lambda_3^2 B_{12}V_{21})}{B_{32}V_{23} + B_{12}V_{21}}. \tag{6.7}$$

We have verified that (6.7) agrees with computer calculations of eigenvalues of the linearized equations. Results are similar for a larger number of states, any odd N yielding one $p = 0$ root and one resistive mode of the form

$$p = \tau^{-1}\left(\frac{-\sum \lambda_i^2 a^2 K_i}{\sum K_i}\right) \to \tau^{-1}\frac{\Delta' a^2}{w_L}, \tag{6.8}$$

where we have restored dimensional constants, giving $\tau = a^2\mu_0/\eta$, the K_i being ever more complicated functions of the $\delta\mathbf{W}$ matrix elements as N increases. Note the similarity to the analytic form of the resistive mode growth constant. The λ^2 weighting (from integrating $\boldsymbol{\nabla} \times \eta\mathbf{J} \propto \boldsymbol{\nabla} \times \boldsymbol{\nabla} \times \mathbf{B}$) corresponds to Δ' in analytic

https://doi.org/10.1017/S0022377801001416 Published online by Cambridge University Press

Table 2. Linear growth rates for two equilibrium cases. Case 1: $a_1 = 0$, $a_2 = 0$ and $a_3 = 1$. Case 2: $a_1 = 1$, $a_2 = 0.05$ and $a_3 = 0.09$.

		Case 1		Case 2	
m	n	γ at $\eta = 0$	γ at $\eta = 10^{-5}$	γ at $\eta = 0$	γ at $\eta = 10^{-5}$
1	1	1.78×10^{-1}	1.81×10^{-1}	0	1.98×10^{-3}
1	0	5.47×10^{-2}	6.62×10^{-2}	0	5.56×10^{-5}
1	−1	0	1.42×10^{-2}	5.61×10^{-3}	6.21×10^{-3}
1	−2	0	5.42×10^{-3}	0	0
1	−3	0	0	0	0
2	−5	0	0	0	0

theory, giving the theoretical tearing growth rate on the right with resistive layer half-width $w_L = (\gamma\eta)^{1/4}$ in our units.

7. Benchmarks

We have benchmarked our code to the textbook case of an axisymmetric equilibrium in cylindrical geometry with constant λ, finite resistivity η and zero viscosity ν, for which linear growth rates can be calculated analytically (Gibson and Whiteman 1968). Though λ is constant, for unrestricted k_z resistive tearing sets in at $\lambda = 3.104$, at which point the axisymmetric state ceases to be the state of lowest magnetic energy: typically the highest λ value observed in RFPs (Taylor 1986). Ideal MHD instability sets in at a somewhat higher $\lambda = 3.176$. For our benchmark equilibrium, we choose the symmetric state **3** in Table 1 with $\lambda = 5.52$, well above both of these thresholds.

To guide our choice of perturbation states, we first calculate linear growth rates using a code that finds the eigenfrequencies p for the matrix equations of Sec. 6 linearized around the benchmark equilibrium state **3**. Results are shown in Table 2, case 1, for several (m, n) resonances. For these calculations, 19 radial eigenstates are retained for each resonance, being the first 19 states for a given m and n in ascending order of values of λ for that resonance. For example, for the resonance with $m = 1$ and $n = -1$ (denoted as $(1, -1)$), the lowest radial state is state **4** in Table 1 and the third highest is state **6**, both of positive parity. (Parities alternate in sign with ascending λ.) Growth rates γ are shown for $\eta = 0$ and for finite $\eta = 10^{-5}$. Tearing modes are resonances for which $\gamma > 0$ only if $\eta \neq 0$, while resonances giving instability even if $\eta = 0$ are ideal MHD modes for which finite η merely gives a small correction to the growth rate.

7.1. Island growth

As a benchmark, we calculate island growth for the $(1, -1)$ tearing mode in Table 2, case 1, keeping only perturbations associated with this mode (states **4**, **5** and **6** together with the other 16 radial eigenstates for this mode not shown in the table). Results are given in Fig. 2, showing exponential growth from 'noise' consisting of all 19 magnetic perturbation states set at initial amplitude $a_i = 10^{-4}$ (energy $a_i^2 = 10^{-8}$). Note that only states **4** and **6** actually grow to saturation.

The growth of the island is shown in cross-section in Fig. 3. This island structure is formed by the sum of the dominant states in Fig. 2, namely the symmetric state **3** together with perturbation states **4** and **6**. All other perturbation states are too

https://doi.org/10.1017/S0022377801001416 Published online by Cambridge University Press

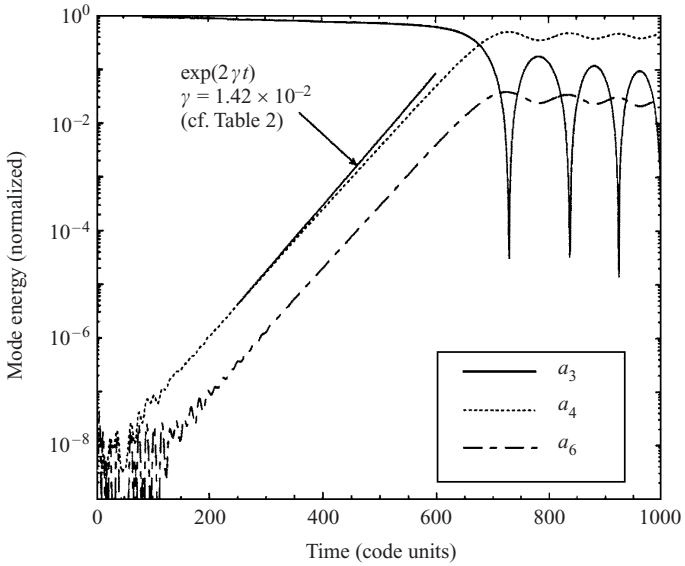


Figure 2. Mode energy versus time for a driven spheromak, showing growth and saturation of $m = 1$, $n = -1$ modes.

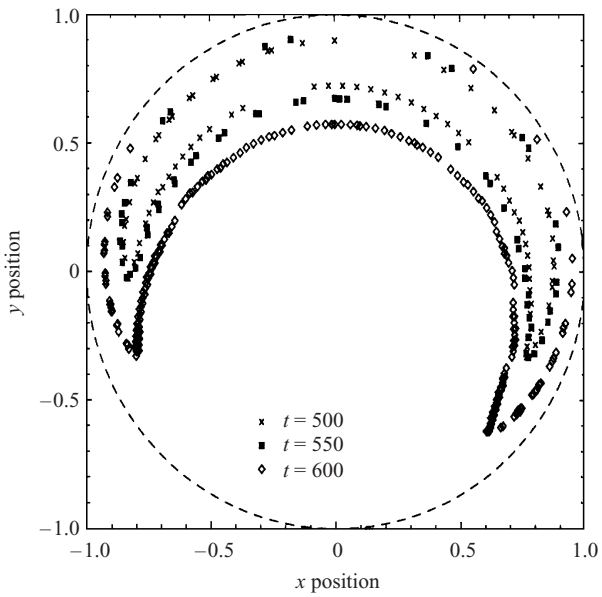


Figure 3. Puncture plot of magnetic field at various times, showing island growth.

weak to contribute. The width w of the island agrees with the well-known analytic formula $w/a = [(\delta B/B)/(q'a)]^{1/2}$ if we take $\delta B = a_4$ for the dominant mode, q' being the radial derivative of the safety factor $q = rB_z/aB_\theta$ for equilibrium state **3**.

The saturation exhibited in Fig. 2 is quasilinear saturation, since to date we have only calculated the quasilinear approximation to (2.6) and (2.7), as noted in Sec. 4.

https://doi.org/10.1017/S0022377801001416 Published online by Cambridge University Press

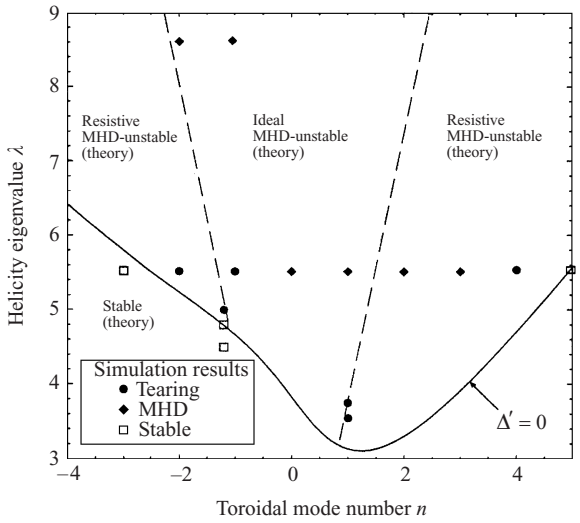


Figure 4. Benchmark test of code with single-helicity equilibrium, compared with analytic theory.

Higher-order corrections are required to observe Rutherford secular growth of the island, giving $\delta B \propto t^2$ when the island width $w > w_L = (\gamma\eta)^{1/4}$ (Rutherford 1973).

7.2. Convergence

The emergence of just two perturbation states, states **4** and **6** in the example shown in Fig. 2, suggests that only a few radial states need be retained in the Galerkin approximation to recover tearing island growth. Calculations with fewer radial states (as low as 7) and more states (up to 25) give similar results. Thus we conclude that only a few states are required to produce island structures, given a tearing-unstable starting point.

The threshold for tearing instability is a more delicate question, even in analytic theory, especially in the transition from tearing to ideal modes occurring when $B_r = 0$ at resonance so that $\Delta' \to \infty$. Stability thresholds for our Galerkin solutions are shown in Fig. 4, illustrating example points of stability, tearing instability and ideal MHD instability in λ–n space, together with stability boundaries from linear theory (Gibson and Whiteman 1968). The Galerkin stability boundaries are qualitatively similar to the theory but not exactly so: for example, our $(1, -1)$ tearing mode is MHD-unstable according to the theory.

The magnitudes of tearing growth rates shown in Table 2, of order 0.01, are similar to those for the analytic theory, but again exact correspondence is elusive. Galerkin growth rates for the $(1, -1)$ tearing mode are plotted in Fig. 5 for a range of η values and 7, 19 and 25 radial perturbative states. The curves for 19 radial states and 25 radial states are similar. Shown for comparison is the analytic result $\gamma \propto \eta^{3/5}$, arbitrarily scaled to our result at $\eta = 10^{-7}$. The $\eta^{3/5}$ scaling corresponds to a linear width $w_L = (\gamma\eta)^{1/4}$ in (6.8).

Convergence of results is faster for a small odd number of modes, as opposed to a small even number of modes, due to the aliasing phenomenon characteristic of Galerkin-type algorithms discussed in Sec. 6. For the cases studied here, where a small odd number of modes were used, the results were tested for short integra-

https://doi.org/10.1017/S0022377801001416 Published online by Cambridge University Press

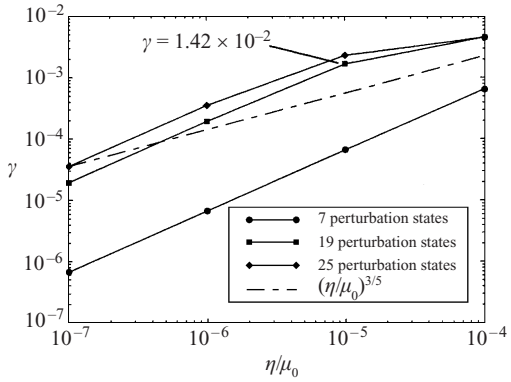


Figure 5. Calculated growth rate γ versus resistivity η.

tion times against a case where a large number of modes were retained. Similar performance was obtained, indicating that a small odd N could be safely used.

We believe the degree of agreement with theory found here is satisfactory for our purposes, given the fact that only a few of the radial eigenstates needed to resolve tearing modes in the linear regime actually grow to significant amplitude. Based on these results, we usually retain 19 radial perturbation terms for each (m, n) resonance included in our nonlinear calculations.

8. Quasilinear calculations for a decaying equilibrium

In this section and the next, we describe examples of nonlinear calculations using the spectral code, presently in the quasilinear approximation as discussed in Sec. 4.

We first calculate the time evolution of an equilibrium state after the gun is turned off. We again set the viscosity $\nu = 0$, but we retain a finite resistivity η required for tearing modes. Because of resistivity, the state decays as it evolves, and the flux core shown in Fig. 1 would disappear, leaving only the spheromak core that is well described by our straight-cylinder approximation, as discussed in Sec. 3.

The spectral states employed include those listed in Table 1, with eigenvalues satisfying spheromak-like boundary conditions discussed in Sec. 4. The three symmetric states from which we construct the initial equilibrium state are listed first in the table. The lowest state, **1**, is the 'Taylor state' with $\lambda = 2.405$, as noted earlier. This state is stable to all modes, its eigenvalue lying below the threshold $\lambda = 3.104$ for tearing instability of a symmetric state with constant λ as discussed in Sec. 7.

Instability becomes possible when we include contributions from state **2** with $\lambda = -2.045$ and state **3** with $\lambda = 5.520$, the benchmark case, which is unstable by itself. Though individually these eigenstates have zero pressure and constant λ, their weighted sum can have finite pressure as noted previously, and also a non-uniform $\lambda_\parallel = \mu_0 j_\parallel / B$ (and hence non-uniform $q(r)$) that are the potential causes of instability in a spheromak. As initial values of the coefficients we take $a_{\mathbf{1}} = 1.0$, $a_{\mathbf{2}} = 0.05$ and $a_{\mathbf{3}} = 0.09$, chosen to obtain a low value of $\beta = 2\mu_0 p / B^2$ of experimental interest and to construct a realistic $\lambda_\parallel$ profile, as shown in Fig. 6.

As perturbations, we use combinations of the non-symmetric eigenstates shown in Table 1. As noted earlier, the quantum numbers m and n play a special role in determining the location of magnetic resonances where the safety factor $q(r) = -m/n$, denoted hereinafter as the resonance (m, n). As discussed in Sec. 7, we take

https://doi.org/10.1017/S0022377801001416 Published online by Cambridge University Press

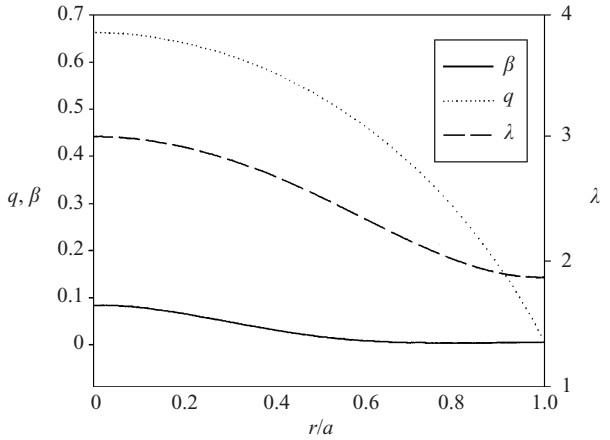


Figure 6. Profiles of q, β and λ for equilibrium used in decaying spheromak calculations.

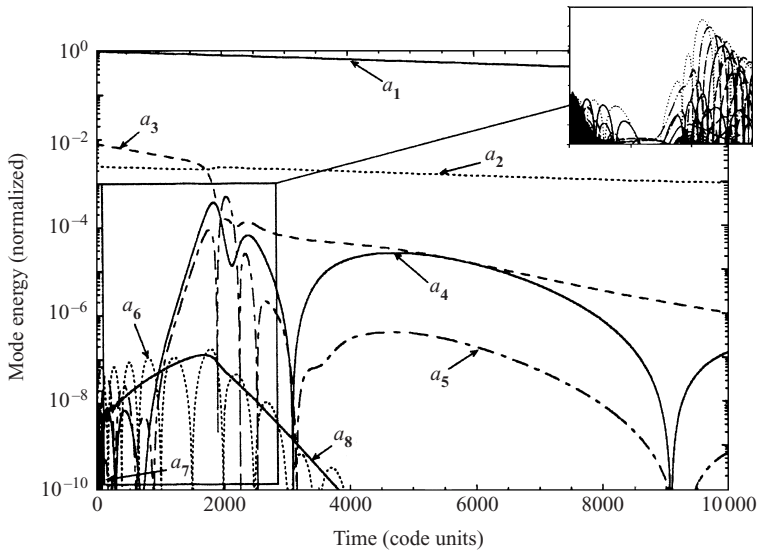


Figure 7. Mode energy versus time for a decaying spheromak.

19 radial eigenstates for each (m, n) magnetic resonance, but only a few of these are listed in the table.

The initial equilibrium has been chosen to be only weakly unstable. Linear growth rates for the initial equilibrium state are shown in case 2 of Table 2, both for finite resistivity ($\eta = 10^{-5}$) and for $\eta = 0$. Note for this case that the $(1, -1)$ resonance is unstable for zero resistivity, giving an ideal MHD mode, while the (1, 1) and (1, 0) resonances that are made unstable by finite η are tearing modes. Note also that eigenstates with large n are stable.

For this exercise, we have included three resonances: the $(1, -1)$ mode that is initially MHD-unstable, the $(1, 1)$ tearing mode, and the initially stable $(1, -2)$ mode. Figure 7 shows the nonlinear evolution from the initially unstable state. The jumble of amplitudes early in time (shown in the inset) includes all 19 radial perturbation states for each resonance included in the calculation. However, only a few pertur-

https://doi.org/10.1017/S0022377801001416 Published online by Cambridge University Press

bative states survive with significant amplitude. Note that it is the squares of the amplitudes that are plotted: the sharp drops in the a_4 curve correspond to a change of sign of the amplitude.

We have also calculated the energy E and helicity K given by (2.9) and (2.10). A good test of numerical convergence of our solutions is given by comparing these results with the conservation laws obtained by differentiating these equations using (2.6) and (2.7), now including resistivity, to obtain

$$\frac{dE}{dt} = -\eta \sum_i \lambda_i^2 a_i^2, \tag{8.1}$$

$$\frac{dK}{dt} = -2\eta \sum_i \lambda_i a_i^2. \tag{8.2}$$

Integrating these equations over time gives results agreeing with those calculated during the run to within 0.5%. Note the direct evidence that K is better conserved than E implicit in the positive weighting factor λ_i^2 in (8.1) versus the factor λ_i in (8.2) which is both smaller in magnitude and of variable sign.

The main conclusion from this preliminary study is that in the quasilinear Galerkin approximation, weak instability does not cause full relaxation to the Taylor state, as evidenced by the finite amplitudes a_2 and a_3 as the state evolves in Fig. 7. Even the initially MHD-unstable amplitude a_4 saturates. At $t = 5000$, all three resonances are stable.

9. Simulation of gun injection

While plasma confinement in a decaying spheromak may be of interest for pulsed reactor scenarios (Fowler et al. 1999), in recent years attention has focused on the possibility of sustaining a spheromak by continuous injection by a magnetized Marshall gun (Jarboe 1994; Hill et al. 2000). Unlike inductively driven RFPs and tokamaks, the axisymmetric spheromak configuration in Fig. 1 cannot be maintained in steady state by electrostatic gun injection, by Cowling's theorem (Sovinec et al. 2001). Nonetheless, as was discussed in Sec. 1, it has been supposed that a gun could sustain a quasisteady state by a continuous process of magnetic relaxation whereby instability in the gun current passing through the flux core of Fig. 1 propagates helicity into the surrounding spheromak (Jensen and Chu 1984).

During the course of our work, numerical calculations of gun injection into spheromaks have been published that call this relaxation model into question (Sovinec et al. 2001). These studies employ the NIMROD code to solve numerically (2.1) and (2.2), including also the inertial term omitted here. The axisymmetric component of the field in the NIMROD solutions resembles Fig. 1, but the system actually evolves to a stable d.c. state in which, in three dimensions, all field lines carrying current are attached to the gun, as they must be in an electrostatically driven steady state. Velocity flows play an important role in these solutions, as they do for inductively driven steady states (Montgomery and Shan 1994; Montgomery et al. 1999). It is the symmetrically averaged $\mathbf{v} \times \mathbf{B}$ term in Ohm's law that provides the loop voltage needed to sustain a symmetrically averaged flux core configuration in this case.

Here we present our first attempt to simulate gun injection using the Galerkin approximation. We continue to use the straight-cylinder representation of the sphero-

https://doi.org/10.1017/S0022377801001416 Published online by Cambridge University Press

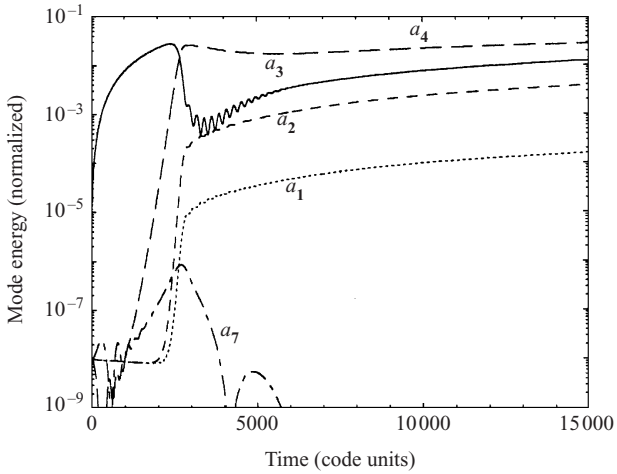


Figure 8. Mode energy versus time for a gun-driven spheromak.

mak core, as shown in Fig. 1. This model does not include the gun-driven flux core, to which the spheromak is coupled through instability. To represent this coupling, we focus on the symmetric eigenstate **3** in Table 1, which, as noted earlier, is unstable by itself, with growth rates given in case 1 of Table 2. We represent coupling to the flux core by adding a source term s to the evolution equation for the state **3** amplitude, giving, by adding this term to (2.6),

$$\frac{\partial a_{\mathbf{3}}}{\partial t} = \sum_{j,k} \lambda_{\mathbf{3}} v_j a_k M_{ijk} - \eta \lambda_{\mathbf{3}}^2 a_{\mathbf{3}} + s. \tag{9.1}$$

All other symmetric and perturbative states will continue to be represented by (2.6) and (2.7) with no source term. We again take the viscosity $\nu = 0$, except as noted in Sec. 9.3.

We can regard the source as representing $s = \int dV\, \mathbf{B}_i \cdot \mathbf{E}$ where $\mathbf{E}$ is an effective electric field accomplishing the coupling. We will take s constant in time, roughly approximating a constant gun voltage producing a continuous helicity input to the spheromak (time-averaged). In most of our calculations, we have taken very small initial values for all three equilibrium components, so that the growing state **3** is unstable early in the calculation, whereas in actual gun injection the gun current only becomes unstable when the current exceeds a threshold determined by the bias field. Our spectral representation does not yet include a bias field. However, we find that the asymptotic state obtained with constant s is not sensitive to initial conditions.

9.1. Driven tearing modes

Figure 8 gives results keeping only perturbations for which the symmetric state **3** is by itself tearing unstable, with lowest-lying radial states **4** and **7** for the $(1, -1)$ and $(1, -2)$ tearing modes shown in Table 2, case 1. By 2000 time units, the $a_{\mathbf{1}}$ 'Taylor-state' amplitude and also the $a_{\mathbf{2}}$ symmetric-state amplitude have begun to grow, but the tearing 'perturbative' mode amplitude $a_{\mathbf{4}}$ grows to an even higher level, actually exceeding the driven-state amplitude $a_{\mathbf{3}}$.

Figure 9 gives the time evolution of energy and helicity for this case. Again

https://doi.org/10.1017/S0022377801001416 Published online by Cambridge University Press

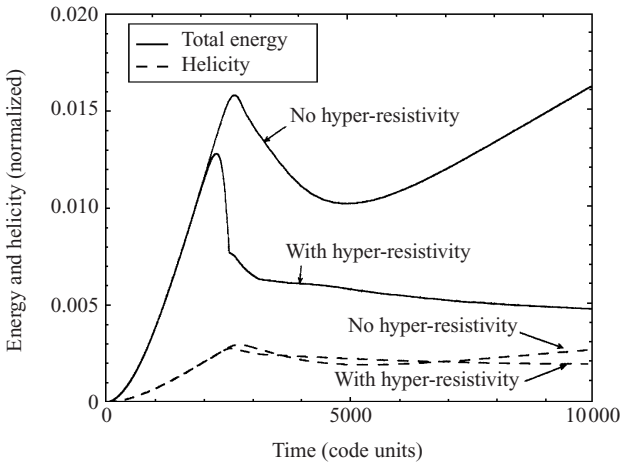


Figure 9. Total energy (magnetic plus kinetic) and helicity for the simulations shown in Figs 8 and 10.

we have checked energy and helicity conservation, now adding the source terms to (8.1) and (8.2), and again these quantities are conserved to within 0.5%. The magnetic energy accounts for almost all of the total energy, indicating that the **v** perturbation remains very small, which we also verified directly. While individual terms in the **v** equation are large, they almost cancel, equivalent to neglecting inertia in calculating the 'outer' solution in analytic treatments of tearing modes. Nonetheless, finite **v** is essential here, as it was in NIMROD steady-state solutions.

Somewhat like the NIMROD results cited above, we see that, in contrast with Fig. 7, in which perturbative amplitudes oscillate in sign, in Fig. 8, the dominant eigenstate amplitudes are approaching a relatively steady asymptotic balance, giving evidence of quasilinear saturation of the instabilities long before gun injection comes into balance with dissipation (not yet reached in Figs 8 and 9). This asymptotically stable combination of states is maintained because it is marginally stable to tearing, as evidenced by a large drop in growth constant: down to 10^{-5} at $t = 10\,000$. Though our straight-cylinder model cannot prove it directly, this approach toward a d.c. state is strongly suggestive of open field lines connected to the gun, as in the NIMROD solutions. Given the large magnitude of the non-symmetric a_4 amplitude, the field structure can no longer be described as an 'island', and would instead resemble the highly contorted structures found by NIMROD.

9.2. Effect of kinetic hyper-resistivity

The large asymmetry of solutions found by our code, and in NIMROD, has prompted us to examine physical effects possibly missing from incompressible MHD theory. One of these is kinetic hyper-resistivity of the form (Kaw et al. 1979)

$$E_z = \eta j_z - (rB)^{-1} \frac{\partial}{\partial r}\left(r \frac{B^2 \chi m_e}{ne^2} \frac{\partial \lambda_Z}{\partial r} \right), \tag{9.2}$$

$$\chi = \pi v_e R \left(\frac{\delta B}{B} \right)^2, \tag{9.3}$$

https://doi.org/10.1017/S0022377801001416 Published online by Cambridge University Press

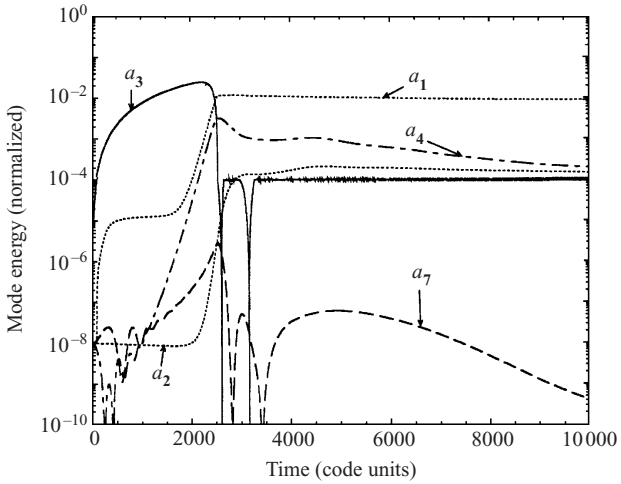


Figure 10. Mode energy versus time for a gun-driven spheromak with kinetic hyper-resistivity.

where χ is a momentum diffusion coefficient taken equal to the Rechester–Rosenbluth turbulent thermal diffusivity (Rechester and Rosenbluth 1978), and the B factors were added by Boozer (1986) to conserve helicity.

As defined in (9.2), hyper-resistivity applies only to the 'mean field', represented here by the symmetric states. Accordingly, to approximate kinetic hyper-resistivity in our code, we add to the right-hand side of (2.6) for $a_{\mathbf{3}}$ a term of the form

$$K_{\mathbf{3}} \frac{\lambda_{\mathbf{3}}}{a_{\mathbf{3}}} \sum_i k_i^2 a_i^2, \tag{9.4}$$

and we add a similar term to the $a_{\mathbf{1}}$ equation, with $K_{\mathbf{3}} = -K_{\mathbf{1}}$ to conserve helicity. (We omit hyper-resistivity in the $a_{\mathbf{2}}$ equation for technical reasons, whereby negative λ causes numerical instability with our simple approximation to (9.2).) With these additions, helicity of the mean field is conserved, but not its energy, as is true also for the analytic expression in (9.2). To approximate a threshold for instability, we turn on hyper-resistivity only after $a_{\mathbf{3}}^2 > 10^{-4}$.

We expect a hyper-resistivity of sufficient magnitude to smooth out the tearing fluctuations on which it depends, introduced here through the factor $k_i^2 a_i^2$ in (9.4) to represent δB^2 in (9.3) together with a factor k_i^2 introduced ad hoc to give greater weight to short wavelengths. To demonstrate this, we have carried out calculations for three cases, with $K_{\mathbf{3}} = 10^{-6}$, 10^{-4} and 10^{-2}. The smallest value yields results similar to those in Fig. 8 with zero hyper-resistivity, while the larger values produce dramatic changes, as shown in Fig. 10 for the case $K_{\mathbf{3}} = 10^{-4}$. Comparing Figs 8 and 10, we see that adding hyper-resistivity increases the fraction of energy going into $a_{\mathbf{1}}$, showing that strong hyper-resistivity drives up the Taylor-state amplitude $a_{\mathbf{1}}$ at the expense of the perturbations, since helicity is conserved overall.

As can be seen in Fig. 10, given strong hyper-resistive coupling out of the driven state $a_{\mathbf{3}}$, the amplitude of this driven state hovers around the threshold at which hyper-resistivity is activated in our model, the time average of its excursions above the threshold accounting for the rate at which helicity is transferred to the $a_{\mathbf{1}}$

https://doi.org/10.1017/S0022377801001416 Published online by Cambridge University Press

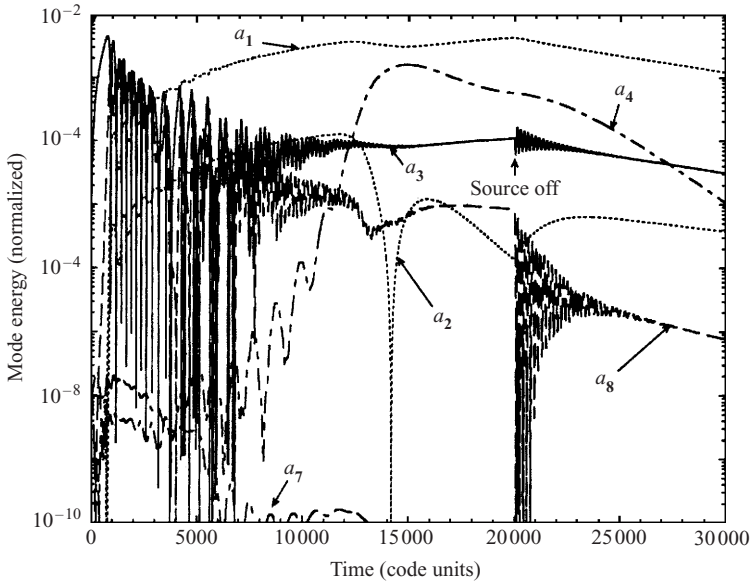


Figure 11. Mode energy versus time for a gun-driven spheromak with ideal MHD mode added.

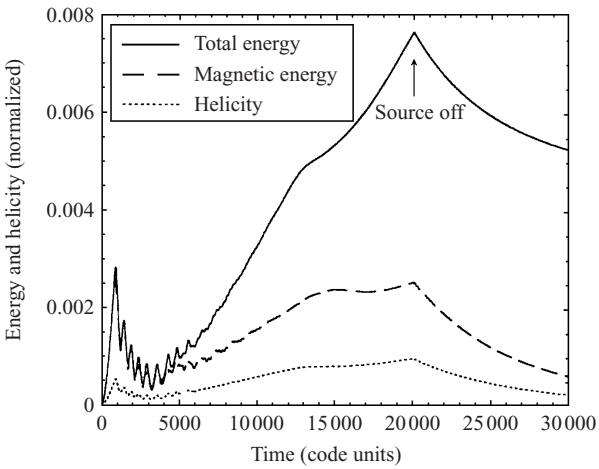


Figure 12. Energy and helicity versus time for simulation shown in Fig. 11.

Taylor-state amplitude. Presumably a similar result would be obtained if the bias field were included, causing a_3 to hover near the stability threshold.

9.3. Driven MHD mode

To explore the ability of the Galerkin method to resolve different timescales, we have repeated the calculations of Sec. 9.1, adding the ideal MHD-unstable (1, 1) resonance from Table 2, case 1. Figure 11 shows the time evolution of the system, now exhibiting rapid oscillation early in time but again indicating an asymptotic approach to a quasisteady composition of states that is marginally stable, with a dramatic drop in growth rate compared with earlier times ($\gamma = 10^{-5}$) before the

https://doi.org/10.1017/S0022377801001416 Published online by Cambridge University Press

gun source term is turned off at $t = 20\,000$. Figure 12 shows the evolution of energy and helicity for this case.

The viscosity is still zero in the results of Figs 11 and 12, and velocity amplitudes (not shown) are now very large, accounting for a large fraction of the energy and representing mass velocities of the order of the actual Alfvén speed characteristic of MHD activity (outside the range of validity of (2.2) and (2.7), in which terms quadratic in $\mathbf{v}$ were omitted). Adding viscosity damps this motion. To exaggerate the effect, we took $\nu = 10^{-4}$ (a magnetic Prandtl number of 10). As expected, the kinetic component of the energy was partially dissipated, giving a much lower total energy, while the magnetic energy and helicity were not much affected. The overall magnetic energy still lies well above the helicity and hence above the Taylor minimum energy (1.2 K in our units).

10. Discussion

A spectral code to study magnetic relaxation in spheromaks has been completed and benchmarked for tearing modes in cylinder geometry. Example calculations have demonstrated the flexibility of the code in exploring physical processes one by one, to determine their effect on relaxation – including processes such as kinetic hyper-resistivity not yet included in numerical MHD codes. We believe that the efficacy of this method in the simple cylindrical geometry shows its applicability to more realistic spherical geometry, explored briefly in (Hua et al. 1998), and this will be a focus of future work.

We would also like to pursue further our work on gun injection in spheromaks, including the as-yet-unexplored effects of viscosity. It is the Hartmann number $\propto (\eta\nu)^{-1/2}$, combining resistivity and viscosity, that determines the stability of dissipative MHD systems (Montgomery 1992; Chen et al. 1990), and viscosity, is known to play an important role in the minimum-dissipation version of relaxation theory (Montgomery and Phillips 1988; Montgomery et al. 1989). The hyper-resistivity discussed in Section 9.2 can itself be viewed as a form of viscosity (Kaw et al. 1979; Boozer 1986). Indeed, electrostatic gun-driven spheromaks, which depend on some such process to maintain closed flux surfaces in quasisteady state, may be the definitive testing ground for these concepts in fusion research.

Acknowledgements

We would like to thank Dr Carl Sovinec for an advance copy of the NIMROD paper cited here and for useful discussions. We would also like to thank the reviewers for helpful suggestions. The work of Dr Hua was supported by Los Alamos National Scientific Laboratory Grant UCRD-STB-UC-99-146.

References

Boozer, A. H. 1986 *J. Plasma Phys.* **35**, 133.
Chandrasekhar, S. and Kendall, P. C. 1957 *Astrophys. J.* **126**, 457.
Chen, H., Shan, X. and Montgomery, D. C. 1990 *Phys. Rev.* **A42**, 6158.
Fowler, T. K. and Hua, D. D. 1995 *J. Fusion Energy* **14**, 181.
Fowler, T. K., Hua, D. D., Hooper, E. B., Moir, R. W. and Pearlstein, L. D. 1999 *Comments Plasma Phys. Contr. Fusion* **13**, 83.
Gibson, R. D. and Whiteman, K. J. 1968 *Plasma Phys.* **10**, 1101.

https://doi.org/10.1017/S0022377801001416 Published online by Cambridge University Press

Hill, D. N., Bulmer, R. H., Cohen, B. I., Hooper, E. B., Lodestro, L. L., Mattor, N. et al. 2000 Spheromak formation Studies in SSPX. 18th International Atomic Energy Agency Fusion Energy Conference, Sorrento, Italy, 4–10 October 2000 (UCRL-JC-13828).

Hua, D. D., Fowler, T. K. and Morse, E. C. 1998 'Evolution of the magnetic field in spheromaks using spectral expansions.' Department of Nuclear Engineering, University of California, Berkeley, September 1998.

Jarboe, T. R. 1994 *Plasma Phys. Contr. Fusion* **36**, 945.

Jardin, S. C. 1982 *Nucl. Fusion* **22**, 629.

Jensen, T. H. and Chu, M. S. 1984 *Phys. Fluids* **27**, 2881.

Kaw, P. K., Valeo, E. J. and Rutherford, P. H. 1979 *Phys. Rev. Lett.* **43**, 1398.

Montgomery, D. C. 1992 *Plasma Phys. Contr. Fusion* **34**, 1157.

Montgomery, D. C. and Phillips, L. 1988 *Phys. Rev.* **A38**, 2953.

Montgomery, D. C. and Shan, X. 1994 *Comments Plasma Phys. Contr. Fusion* **15**, 315.

Montgomery, D. C., Phillips, L. and Theobald, M. L. 1989 *Phys. Rev.* **A40**, 1515.

Montgomery, D. C., Bates, J. W. and Kamp, L. P. 1999 *Plasma Phys. Contr. Fusion* **41**, A507.

Morse, E. C. 1998 *Phys. Plasmas* **5**, 1354.

Patterson, G. S. and Orszag, S. A. 1971 *Phys. Fluids* **14**, 2538.

Rechester, A. B. and Rosenbluth, M. N. 1978 *Phys. Rev. Lett.* **40**, 38.

Rosenbluth, M. N. and Rutherford, P. H. 1981 Tokamak plasma stability. In: *Fusion*, Vol. 1, Part A (ed. E. Teller). New York: Academic Press, Chap. 2.

Rutherford, P. H. 1973 *Phys. Fluids* **16**, 1903.

Shan, X. and Montgomery, D. C. 1993a *Plasma Phys. Contr. Fusion* **35**, 619.

Shan, X. and Montgomery, D. C. 1993b *Plasma Phys. Contr. Fusion* **35**, 1019.

Shan, X., Montgomery, D. C. and Chen, H. 1991 *Phys. Rev.* **A44**, 6800.

Shebalin, J. V. and Montgomery, D. 1988 *J. Plasma Phys.* **39**, 339.

Sovinec, C. R., Finn, J. M. and del-Castillo-Negrete, D. 2001 *Phys. Plasmas* **8**, 475.

Taylor, J. B. 1986 *Rev. Mod. Phys.* **58**, 741.

https://doi.org/10.1017/S0022377801001416 Published online by Cambridge University Press